A multi-physics CFD study to investigate the impact of laser beam shaping on metal mixing and molten pool dynamics during laser welding of copper to steel for battery terminal-to-casing connections

Giovanni Chianese [a], Qamar Hayat [b,*], Sharhid Jabar [b], Pasquale Franciosa [b], Darek Ceglarek [b], Stanislao Patalano [a]

[a] *University of Naples Federico II, Department of Industrial Engineering, P.le Tecchio, 80125 Naples, Italy*
[b] *WMG, The University of Warwick, 6 Lord Bhattacharyya Way, Coventry CV4 7AL, UK*

ARTICLE INFO

ABSTRACT

This study aims to investigate the impact of laser beam shaping on metal mixing and molten pool dynamics during laser beam welding of Cu-to-steel for battery terminal-to-casing connections. Four beam shapes were tested during LBW of 300 μm Cu to 300 μm nickel-plated steel. Both experiments and simulations were used to study the underlying physics. A CFD model was firstly calibrated against experiments and then deployed to explore the effect of the increasing ring-to-core diameter, as well as a tandem laser spot configuration. The study showed that metal mixing is influenced by the keyhole dynamics and collapse events, but also there is an intricate interplay between keyhole geometry, fluid dynamics via Marangoni forces and buoyancy forces. Notably, the buoyance forces due to the different densities of steel and Cu, along with the recoil pressure contribute to the upward flow of steel towards Cu, and hence impact meaningfully the material mixing. The study pointed-out that the selection of a custom ring-to-core diameter and ring-to-core power is a decision with a trade-off between the need of stabilising the keyhole dynamics and the need to reduce the mixing. Findings indicated that 350 μm ring and 90 μm core with 30% of ring power (weld configuration C3) resulted in more stable dynamics of the keyhole, with significant reduction of collapse events, and ultimately controlled migration of steel towards Cu. Additionally, the pre-heating approach with the tandem beam only led to local fusion of Cu and no significant improvement in keyhole stability was observed.

1. Introduction

The push towards net-zero mobility is globally influencing industrial strategies in the automotive sector as reported by IEA (2022). Manufacturers are introducing new vehicles by replacing internal combustion engines with hybrid or fully electric powertrains. The battery pack is a critical component for un-interrupted supply of electricity to e-drives and other electrical systems in electric vehicles (EV). A battery pack typically consists of several battery modules that are electrically connected in series and parallel based on the desired power and capacity requirements (Zwicker et al., 2020). Battery modules hold the battery cells that store the electrical charge and supply it on-demand to the electrical systems. Electrical connections play a critical role in the entire process of battery pack manufacturing since joints with different electrical resistance may result in uneven current loads that can affect the

overall performances of the battery system (Kumar et al., 2021). Joining of dissimilar materials is the most deemed since it complements the properties of the individual materials and allows to develop functionally efficient connections. Joints in EV battery pack involve low-thickness materials (typically 0.3–1 mm) and the welding process is normally performed in lap or fillet configuration. Depending upon design and functional requirements as well as manufacturing costs, research has shown that the following combinations of materials are the most regarded: aluminium (Al) to copper (Cu), steel to Al, Al to steel, Cu to steel (Das et al., 2018).

Connections between Cu and steel have gained much attention in EV applications for joining cells in battery modules. For example, in the cylindrical format, the negative terminals are made of Cu and are generally connected to the steel casing of the cell (Sadeghian and Iqbal, 2022). Several joining processes have been studied for Cu-to-steel welding and they include wire bonding, micro-spot welding,

Nomenclature		P_{sat}	saturation pressure (Pa)
		P_{vap}	partial pressure exerted by vapour (Pa)
ARM	Adjustable Ring Mode	Q_{mass}	evaporation rate (kg/s)
Ar	model parameter to be calibrated (Pa)	R	gas constant (J/mol·K)
CFD	Computational Fluid Dynamics	R_I, R_{II}	curvature radius at interface (m)
c_p c_v	specific heat at constant volume and pressure (J/kg·K)	L_P	Laplace pressure (Pa)
D_{pen}	weld penetration depth (μm)	S_M	Marangoni forces (Pa)
EV	electric vehicle	T	temperature (K)
f	fraction of fluid (-)	T_v, P_v	coordinated of a point on the saturation curve (K, Pa)
IMCs	Inter Metallic Compounds	VOF	volume of fluid
IR	infrared	W_{top}	width of the weld seam at the top (μm)
$\vec{I}$, $\vec{R}$	incoming and reflection vector in the ray-tracing model	W_i	width of the weld seam at the interface (μm)
k	thermal conductivity (W/m·K)	t_{end}	simulated welding time (s)
l_{diff}	thermal diffusion length (m)	α	accommodation coefficient (-)
LBW	laser beam welding	γ	ratio of specific heats of air (-)
$\hat{n}$	normal to surface in the ray-tracing model	ΔHv	latent heat of vaporization (J/kg)
OCT	Optical Coherent Tomography	∇_t	gradient along the tangent direction
P_L	laser power (W)	ρ	mass density (kg/m^3)
P_{recoil}	recoil pressure (Pa)	σ	surface tension (N/m)

ultrasonic welding, micro-TIG welding, electron beam welding and Laser Beam Welding (LBW) (Zwicker et al., 2020). LBW is an attractive option and has recently gained popularity due to advances in versatile methods for laser beam delivery and associated sensors technology for quality control and process monitoring that make LBW comparatively affordable (Kogel-Hollacher, 2020). Brand et al. (2015) demonstrated that LBW is a suitable process for joining battery terminals since it allows the lowest electrical resistance and the highest joint strength, when compared to micro-spot welding and ultrasonic welding; also, it is potentially applicable to any cell configuration and dissimilar metal combinations.

Despite the benefits of LBW, opening and maintaining a stable molten pool on the Cu-side is challenging when using LBW with infrared sources. The absorptivity of Cu at ambient temperature is approximate 5% and increases with rising temperature, and it suddenly jumps up when the melting temperature is reached. A problem with this is that when fusion of the material does happen, a surplus of energy flows through it, which can vaporise the material and create spatters, as well as pores inside the joint. These defects can reduce the electrical conductivity of the joint. At first sight, the solution to the low coupling efficiency of Cu is to switch from infrared sources to visible sources. The absorption increases drastically up to 60% when using visible sources. Green (515 nm) or blue (450 nm) lasers have been investigated by Kogel-Hollacher et al. (2022) and proved that lower power needed for same penetration achievable with infrared lasers and less thermal damage to enamel and insulators. Hummel et al. (2020) experimentally evaluated and proved the beneficial effects of blue laser during laser micro-welding of Cu, and achieved high welding speed with low input power. Nonetheless, compared to infrared lasers, the higher cost, lower plug efficiency and lower beam quality of visible lasers, push practitioners towards the use of multi-kW infrared sources at very high brightness for Cu welding.

In addition to the challenge posed by the laser beam coupling to the Cu, the welding of Cu to steel presents a series of problems. First, they are quite different in terms of physical properties such as density, melting points and thermal expansion and make defect-free welding difficult. Second, although Cu-Fe alloys are completely miscible in the stable liquid state and do not form brittle intermetallic compounds, the system shows a wide metastable miscibility gap at an undercooling level. The liquid phase separation occurs as the liquid cools in the miscibility gap resulting in the supersaturation of one or both liquids. Jeong et al. (2020) has shown that increasing the content of Fe tends to

improve the mechanical properties of alloys but reduce electrical conductivity and ductility. Chen et al. (2013) proved that the toughness and fatigue strength of the joint decreases with the increase in the amount of molten Cu into the steel. Thus, melting of Cu was suggested to be kept at a minimum. Third, excessive penetration of Cu in grain boundaries of steel may result in cracks in the heat affected zone and fusion zone, and ultimately reducing structural performance of the joint. Therefore, to reduce these issues, controlling the mixing of Cu and steel in the molten pool is quite important for producing sound joints.

Laser beam shaping is gaining popularity since it holds the promise to control cooling rates and thermal gradients in and around the molten pool. This theoretically leads to a tailored material response to the heat input both spatially and temporally. A tailored power density profile (Fig. 1 shows typical power density profiles obtained via adjustable ring-mode laser) is generated via adequate insertion of optical components (specially coated lenses of silica substrate) in the optical chain of the welding head; or by electro-optical switching multiple laser beams generated in the laser source itself and enabled by beam combiners with optical phased array. Research has confirmed a positive effect of the laser beam shaping on the control of the weld profile and keyhole stabilization with suppression of spatters and significant reduction of porosity in the weldments. Caprio et al. (2023) investigated the use of beam shaping and beam oscillation to weld 0.2 mm Ni-plated steel sheets in lap joint configuration, which are materials commonly involved in cell to busbar connections. Sokolov et al. (2021) employed the ARM laser coupled with Optical Coherent Tomography (OCT) in Al-to-Cu thin sheets and observed that the use of combined core and ring-shaped laser beams reduced the fluctuations of the keyhole, improved the stability, and ultimately the accuracy of OCT measurements. Rinne et al. (2022) studied the effect of different power distributions between the inner core and outer ring-shaped laser beams on spatter ejection and penetration depth during welding of Cu sheets. Wagner et al. (2022) investigated and proved the influence of dynamic beam shaping on the geometry of the keyhole during welding of Cu by varying the patterns of the intensity distribution in longitudinal and transversal direction. Prieto et al. (2020) implemented dynamic laser beam shaping with infinite pattern and assessed quality of weld seam in 0.8 mm Al thin-sheet and observed that tailored beam with shape frequency over 10 kHz enables welding speed up to 18 m/min with stable keyhole.

Despite the benefits, laser beam shaping introduces new set of parameters and finding the optimal combination of number of beams,
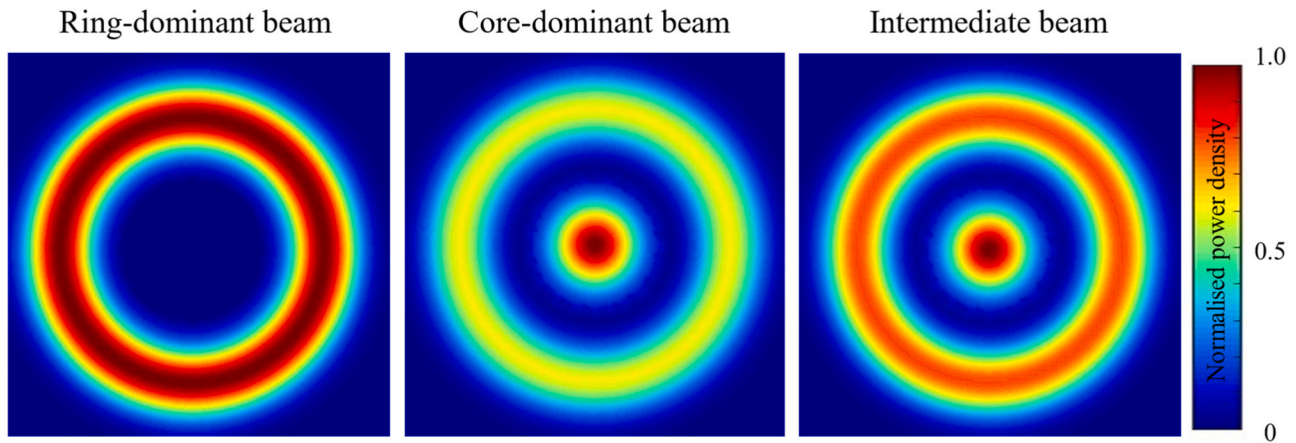
Ring-dominant beam   Core-dominant beam   Intermediate beam

Fig. 1. Example of laser beam shapes obtained via an adjustable ring-mode laser.

shape of beams (multiple spots, C-spot, ring-core spots, pyramid, infinity, spiral shapes, etc. (Prieto et al., 2020)) can be expensive and time consuming since it may require dedicated equipment, expertise and experimental setups. In this context, multi-physics computational fluid dynamics (CFD) enable simulations of the process to reproduce mechanisms which are difficult to observe with in-situ investigations. With the raise of computational power and multi-core computing on high performance clusters, advanced simulations of LBW processes are now a close reality. Huang et al. (2020) developed a CFD model in FLOW-3D WELD® to study the metal mixing during linear laser welding of 200 μm Al to 500 μm Cu with different levels of laser power and velocity of the laser spot. They analysed the contribution of recoil pressure and Marangoni effect on the overall mixing process. Chianese et al. (2022) developed a multi-physics model using FLOW-3D and FLOW-3D WELD® to investigate the effect of part-to-part gap in LBW of Cu-to-steel thin sheets with beam wobbling. They showed that the presence of part-to-part gap and mixing mechanism between parent metals are linked, and the occurrence of part-to-part gap influences the temperature and velocity fields in the molten pool resulting in different mixing mechanisms. However, they did not implement any strategies for weld improvement. Drobniak et al. (2020) and Buttazzoni et al. (2021) implemented CFD multi-physics simulations of 1 mm-thick stainless steel plates with adaptive mesh refinement to predict the shape of the weld seam in presence of part-to-part gap, and they predicted the effect on the process of secondary laser beams with different shapes to optimize the weld quality. Recently, Huang et al. (2023) combined experimental approach and CFD simulations in FLOW-3D WELD® to reveal the effect of oscillation frequency and amplitude on fluid-flow and metal mixing during laser welding of 200 μm Al to 500 μm Cu with circular beam wobbling implemented. Additionally, they implemented a Scheil solidification model to predict the phase distributions in the welds based on the predicted thermo-solute conditions.

While significant research has been already developed using linear laser welding or laser welding with wobbling for joining of dissimilar materials, a clear understanding of metal mixing and dynamics of the keyhole during Cu-to-steel welding with beam shaping are not clearly reported. Research into application of beam shaping for Cu-to-steel welding entails a promising prospect for further development and investigation. Furthermore, the use of advanced CFD models is a viable approach to complement experimental investigations and explore weld configurations with different beam shaping profiles that would be difficult to achieve only with experimental work. Therefore, this paper aims to study the impact of laser beam shaping on metal mixing and dynamics of the keyhole during LBW of Cu-to-steel for battery terminal-to-casing connections. Four beam shapes were tested during LBW of 300 μm Cu to 300 μm nickel-plated steel. Both experiments and CFD simulations were used to study the underlying physics. A CFD model was firstly calibrated against experiments and then deployed to explore the effect of the increasing ring-to-core diameter, as well as a tandem laser spot configuration.

2. Experimental design and model description

2.1. Experimental design

Materials used in this work are Copper SE-Cu58 2.0070 and Nickel-plated steel (commercial name: Hilumin TATA STEEL). Experiments consisted of 25 mm long welds in lap joints configuration with 300 μm Cu on top of 300 μm nickel-plated steel.

Dimensions of the specimens were 65 mm × 30 mm. The laser source used was the Lumentum CORELIGHT, having 55 μm core diameter and 220 μm ring diameter, and BPP 1.4 mm·mrad and 11 mm·mrad for core and ring, respectively. The laser fiber was coupled to the Scout-200 (Laser and Control K-lab, South Korea) scanner to deliver the laser power to the specimens via 2D F-theta scanner with telecentric lenses. Fig. 2 shows the welding setup and specifications of the equipment are in Table 1. Caustic parameters were measured using PRIMES GmbH measurement system.

Each weld seam was cut and prepared to obtain two cross sections for each experiment – cross sections were positioned at 10 mm and 15 mm away from the weld start. Three replicates were performed for each weld configuration. Sectioned samples were mounted in Bakelite resins and standard metallography procedure was performed for grinding and polishing to reveal weld profile under Nikon Eclipse LV150N optical microscope. To evaluate and characterize metal mixing with parent metals, elemental mapping of cross-sections was performed with an FEI Versa 3D dual beam scanning electron microscope using Energy Dispersive X-ray Spectroscopy (EDS mapping).

Welding experiments were performed in continuous power mode without power modulation. The laser beam was focussed perpendicularly on the upper surface of the Cu sheet, and the motion of the laser was linear (no wobbling). Although the use of shielding gas tends to avoid oxidation in the process and reduce hydrogen entrapment, when using scanners to deliver the laser beam, the gas nozzle cannot be positioned in proximity of the beam. Therefore, in this work, all experiments were conducted with no shielding gas. Part-to-part gap was manually checked and set to a nominal zero.

To study the impact of laser beam shaping on metal mixing and molten pool dynamics, 5 weld configurations (C1 to C5) were designed as shown in Table 2, with 4 beam shapes presented in Fig. 3. LBS#1 is single gaussian spot of 90 μm; LBS#2 super-imposes an inner core of 90 μm with an outer ring-shaped profile of 350 μm, with the ring accounting 30% of the total power. LBS#1 and LBS#2 were experimentally tested and enabled by the static beam shaping system of the
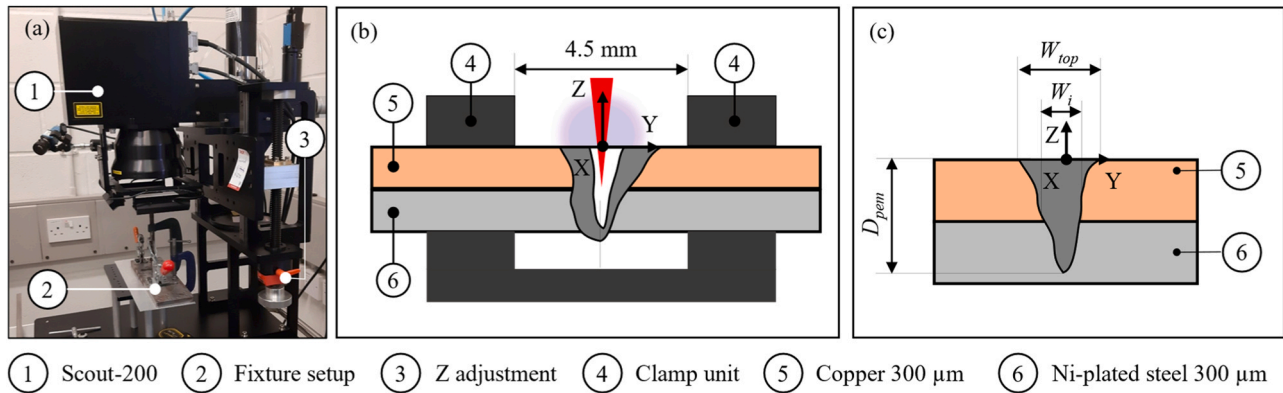
Fig. 2. (a) Welding setup with aluminium fixture; (b) schematical representation of the welding setup; (c) definition of weld features: top weld width, W_{top}; width at the interface, W_i; weld penetration depth, D_{pen}.

Table 1
Specifications of the welding equipment.

Lumentum CORELIGHT		Scout-200, K-lab	
Maximum power	4 kW	Scanning field	70×70 mm²
Wavelength	1070 ± 10 nm	Collimating length	160 mm
Beam Product Parameter (BPP)	1.4 mm·mrad for core and 11 mm·mrad for ring	Focusing length	254 mm
Fiber diameter	55 μm for core and 220 μm for ring	Rayleigh length	0.8 mm

Table 2
Process parameters used for the four selected laser beam shapes in Fig. 3.

| ID	Process parameters		Laser beam shape	Purpose of study
	Laser power [W]	Speed [mm/s]		
C1	600	250	LBS#1	Model calibration with experiments to study metal mixing and molten pool dynamics
C2	830	250	LBS#1	
C3	1530	375	LBS#2	
C4	2500	375	LBS#3	Only simulation to study effect of increased ring-to-core diameter on metal mixing and molten pool dynamics
C5	1100	250	LBS#4	Only simulation to study the effect of pre-heating on molten pool dynamics

Lumentum CORELIGHT source. LBS#3 follows the hollow sinh-Gaussian beam profile as defined in Liu et al. (2019), with 90 μm core and 500 μm ring, with 72% of the total power assigned to the ring. LBS#4 is a

tandem beam with primary (90 μm) and secondary beam (150 μm) at a centre-to-centre distance of 300 μm, and 50% split of the power between primary and secondary beams – LBS#4 was introduced with the aim to increase the absorption rate by the pre-heating action of the secondary beam. LBS#3 and LBS#4 were only simulated since the laser beam shaping of the Lumentum CORELIGHT was only capable to work with fixed core-to-ring diameter ratio. Therefore, only a simulation-based approach (with the model pre-validated and calibrated in C1, C2 and C3) was deemed appropriate in this case to explore the effect of the increasing ring-to-core diameter and tandem laser spot configuration on material mixing.

The power and speed of C1, C3, C4 and C5 were selected with an iterative process to ensure weld penetration depth, D_{pen}, ranging 400 – 500 μm. The choice of this penetration depth is based on the requirement that the temperature at the lower end of the steel sheet remains below 550 K. This precautionary measure aims to prevent any potential damage to the battery cell. Additionally, to minimise the effect of the weld depth on the metal mixing, a uniform depth of penetration was adopted across the different beam shapes for comparative analysis. Welding speeds were kept between 250 mm/s and 375 mm/s which is in line with the experimental work in (Perez Zapico et al., 2021). C2 is a variant of C1 and corresponds to a fully penetrated weld. Although fully penetrated welds must be avoided during LBW of battery terminals due to the risk of fire ignition, this work presents this variant for two reasons: first, to generate an additional weld configuration to validate the simulation; second, to discuss how the metal mixing behaves when transitioning from partial penetration to full penetration.

2.2. Model description

A multi-physics model was developed using the commercial CFD code FLOW-3D® (solver version: 12.0.2.01) and its module FLOW-3D® WELD (release: 7, update: 1). In order to develop a numerical model
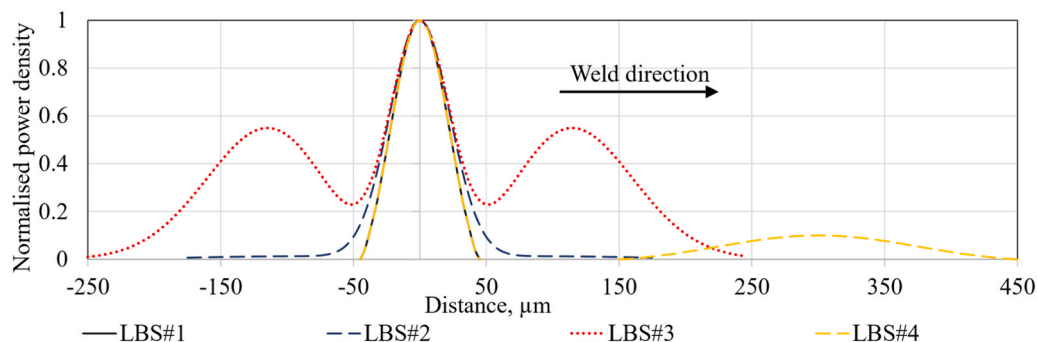
Fig. 3. Normalized power density distribution for LBS#1, LBS#2, LBS#3 and LBS#4.

representing the essential physics during LBW of Cu-to-steel, the following assumptions were considered: (i) the liquid flow is considered Newtonian and incompressible; (ii) volumetric thermal expansion of the liquid metal due to temperature-dependent mass density is accounted; (iii) the air and vaporized metal are modelled as "void" type, with ambient temperature and pressure assigned to model the heat exchange with the metal as a natural convective flux (irradiance is neglected); (iv) the heat sinking effect of the clamping mask is neglected due to the clearance between the weld seam and the mask itself as already presented in (Chianese et al., 2022); (v) the effect of plasma plume on laser absorption is not directly modelled but is accounted in the calibration process as also proposed in previous studies by Lin et al. (2017) and Hao et al. (2021); furthermore, the laser absorption is assumed temperature dependent for Cu, constant for steel, and independent of the incidence angle. This assumption is in-line with the work presented by Huang et al. (2020), where they used the build-in ray-tracing function in FLOW-3D® WELD to predict the laser absorption in the keyhole.

2.2.1. Governing equations, boundary conditions and material properties

To reduce the computational cost of the simulations, the computational domain was divided in two zones (Fig. 4): (1) a process zone which was interested by phase change, and, (2) a thermal diffusion zone that models heat transmission in the sheets. A finer mesh size was used for cells in the process zone, and a mesh size 5 times greater than in the process zone was used for cells in the thermal diffusion zone.

Dimensions of the process zone are 2 mm × 0.8 mm× 0.775 mm. The length (2 mm) of the process zone was chosen to enable the simulation of approx. 1.8 mm weld length, which was experimentally evaluated to be sufficient for reaching the steady-state regime. The width (0.8 mm) of the process zone was selected to ensure that the molten pool was contained in it; the height of the computational domain was chosen equal to 0.8 mm so that, beside the stacked thickness of the processed sheets (0.6 mm), 0.2 mm of air (void type) are included in the computational domain. Extension of the thermal diffusion zone is calculated according to the Eq. (1), where k is the thermal conductivity, c_p the specific heat at constant pressure, ρ the mass density, t_{end} the simulation time, T the temperature, and $T_{amb} = 20\ °C$ the ambient temperature. The simulation time, t_{end}, is function of the welding speed and the weld length (1.5 mm).

$$l_{diff} = 2\sqrt{2\frac{k(T = T_{amb})}{c_P(T = T_{amb}) \bullet \rho(T = T_{amb})} \bullet t_{end}} \tag{1}$$

Four different values of the mesh size in the process zone were considered during sensitivity analysis, namely 40 μm, 20 μm, 15 μm, and 10 μm, that resulted in mesh independent solution for mesh size equal to or below 15 μm, which therefore is the selected size. This led to total number of cells approximately equal to 528 thousand. The geometry of the thin sheets has been modelled in the computational domain, so that in-plane dimensions were parallel to X and Y axis, as shown in the top and side view in Fig. 4(a) and (b). Welding direction was parallel to X axis.

The following physics have been accounted to model the welding process: continuity, fluid flow via Navier-Stokes equations, energy conservation, evaporation, keyhole formation and evolution, solidification, species conservation and tracking, surface tension with Marangoni and Laplace forces and multiple reflections.

Phase change - Eq. (2) governs the evaporation phenomena which are modelled as mass transfer between the liquid phase and the void type and are proportional to the difference between the saturation pressure P_{sat} and the partial pressure P_{vap}. In this equation, α is the accommodation coefficient, R is the gas constant, and T is the temperature. The saturation pressure is calculated as a function of the temperature according to the Clapeyron equation (Eq. (3)), in which the couple (P_v, T_v) represents a point on the saturation curve; γ, c_v, and ΔH_v are the specific heats ratio, the specific heat at constant volume, the latent heat of vaporization, respectively.

$$Q_{mass} = \frac{\alpha}{\sqrt{2\pi RT}} \cdot \left(P_{sat} - P_{vap} \right) \tag{2}$$

$$P_{sat} = P_v \cdot \exp\left(\frac{\Delta H_v}{(\gamma - 1) \cdot c_v T_v} \cdot \left(1 - \frac{T_v}{T} \right) \right) \tag{3}$$

Recoil pressure - during laser welding process, intense localised heating of substrate material causes vaporization which results in recoil pressure. This pressure is proportional to the saturated vapor pressure. The relationship between the recoil pressure, P_{recoil}, and the saturated vapor pressure, P_{sat}, depends on the material properties and laser-to-material interaction. Eq. (4) is derived from Eq. (3) with the introduction of two coefficients, A_r and B, that will be calibrated using experimental data.

$$P_{recoil} = A_r \cdot \exp\left(B \cdot \left(1 - \frac{T_v}{T} \right) \right) \tag{4}$$

Tracking of the keyhole - surface of the keyhole is tracked by the volume of fluid (VOF) method (Daligault et al., 2022), which enables the calculation of the interface between the liquid metal and the void type, according to Eq. (5).

$$\frac{\partial f}{\partial t} + \nabla\left(\vec{V} f \right) = 0 \tag{5}$$

The interface between the cell is tracked using a scalar value f that indicates the fraction of fluid in it. A value of $f = 0$ indicates that the cell has only void, conversely, $f = 1$ corresponds to the case of a cell full of liquid, whereas the case of $0 < f < 1$ indicates that the cell has both the liquid and the void type, and therefore the interface between the two falls in it. Similarly, metals involved in the welding process with fluid flow and mixing are tracked in each cell by means of a scalar value f_2,
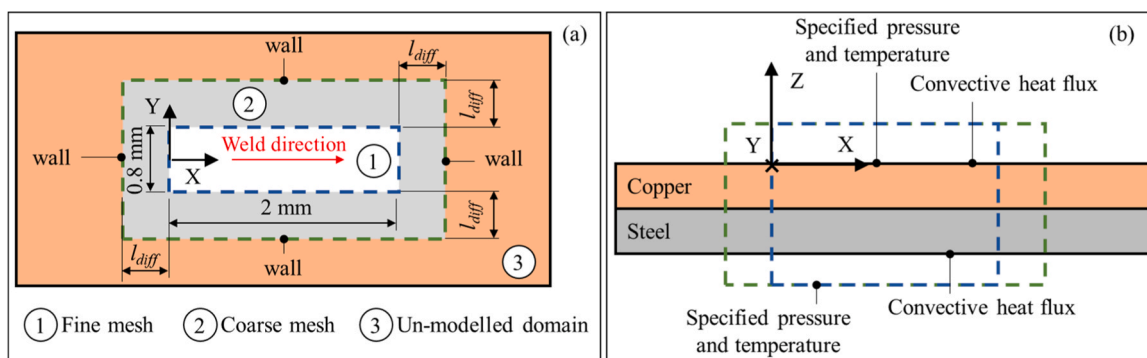

Fig. 4. Top view (a) and side view (b) of a schematic representation of the computational domain and modelling approach with nested meshes (process zone and thermal diffusion zone).

which indicates the fraction of second material within the cells. Values of the generic material property $\overline{\varphi}$ in each cell is evaluated as weighted sum of the properties φ_1 and φ_2 of parent metals based on their mixing, as in Eq. (6).

$$\overline{\varphi} = (1 - f_2) \cdot \varphi_1 + f_2 \cdot \varphi_2 \tag{6}$$

Multiple reflections - Multiple reflections are implemented using a discrete grid cell system through the ray tracing technique. The laser beam is divided into a finite number of rays, which move in the laser beam irradiation direction. When the ray encounters the surface of the material, it is reflected according to vector Eq. (7), in which $\vec{R}$ is the direction of the reflected vector, $\vec{I}$ the direction of the incoming ray, and $\hat{n}$ the normal direction of the material surface.

$$\vec{R} = \vec{I} - 2\left(\vec{I} \cdot \hat{n}\right)\hat{n} \tag{7}$$

Laplace pressure and Marangoni effect - Recoil pressure contributes to the formation of the keyhole and mainly contributes to the velocity field in the fluid; however, surface tension-related phenomena such as Laplace pressure L_P and the Marangoni force S_M have great influence on the overall welding process. Laplace pressure and the Marangoni force are modelled according to Eqs. (8) and (9), in which, σ is the surface tension, R_I and R_{II} are the principal curvature radii, and operator ∇_t indicates the gradient along the tangent direction at the interface. Eq. (9) explicitly indicates the dependence of the Marangoni effect on the gradient of the surface tension, which in assumed temperature-dependent of the surface tension.

$$L_P = \sigma \cdot \left(\frac{1}{R_I} + \frac{1}{R_{II}}\right) \tag{8}$$

$$S_M = \nabla_t \sigma \tag{9}$$

2.2.2. Boundary conditions and material properties

As shown in Fig. (4), the following boundary condition were assigned: wall in the X and Y direction (with constant ambient temperature); assigned pressure and temperature at the boundaries of the computational domain in the Z directions, with natural convective heat flux between the metallic sheets and the air. The heat source was directly imported from the power profiles defined in Fig. 3. Material properties were imported from the JMATPRO® material database. Fig. 5 shows the temperature-dependent plots.

3. Results and discussion

3.1. Model validation

The model has been applied to simulate all the cases listed in Table 2. Model validation was conducted for the weld configurations C1, C2 and C3 by comparing the weld profile in cross sections and Fe concentration line profiles against the experimental results as shown in Fig. 6. Experimental and simulation results show that welding is done through keyhole mode. The generation of a keyhole is significantly influenced by recoil pressure. In the simulation, the recoil pressure is adjusted through the calibration of coefficients A_r and B, as indicated in Eq. 4. During the model calibration process, a value of A_r was determined to be 55,715 Pa, and the parameter B was set to 4, resulting in comparative results with those obtained in experiments. Five different mesh sizes were tested: 20 μm, 15 μm, 10 μm and 5 μm. The choice of the mesh size was driven by the need to have a minimum of 4 cells to discretise the smallest laser spot (i.e., LSB#1 has the smallest beam diameter of 90 μm among the tested beam shapes in Fig. 3). Mesh-independent solution was achieved with mesh size of 15 μm and this led to approximate a million cells in the whole computational domain.

The correlation was conducted looking at two cross-Section (10 mm 15 mm away from the weld start and end) – this was motivated by the need to take into account the experimental errors during the calibration
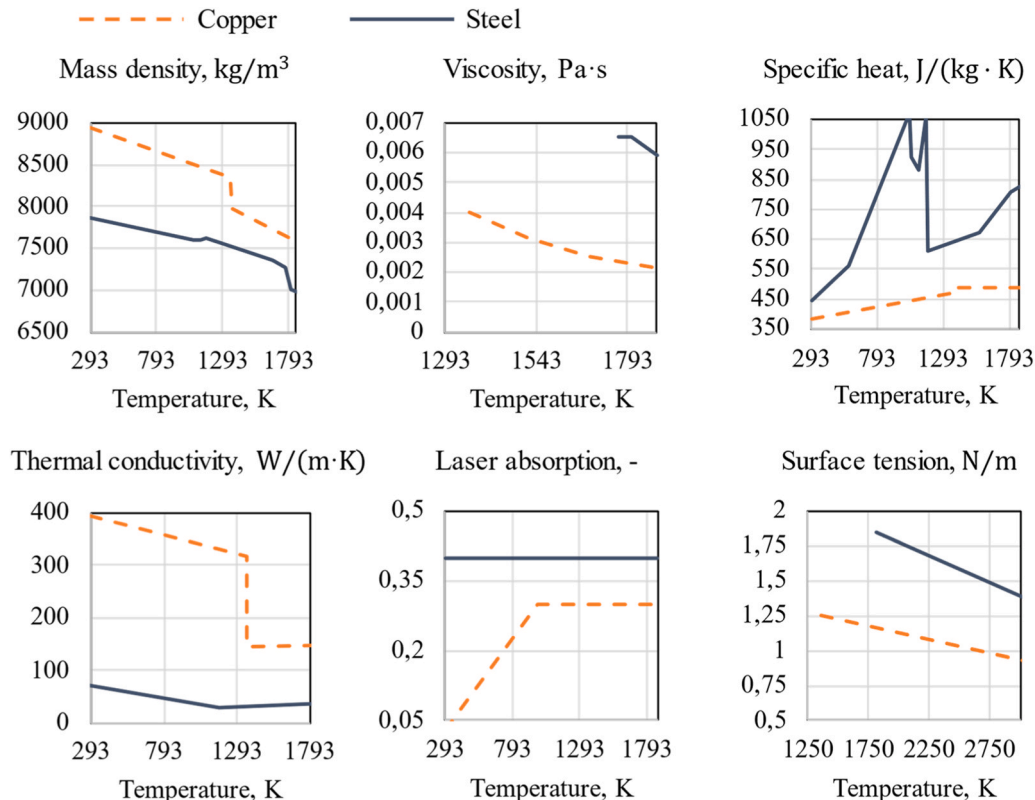

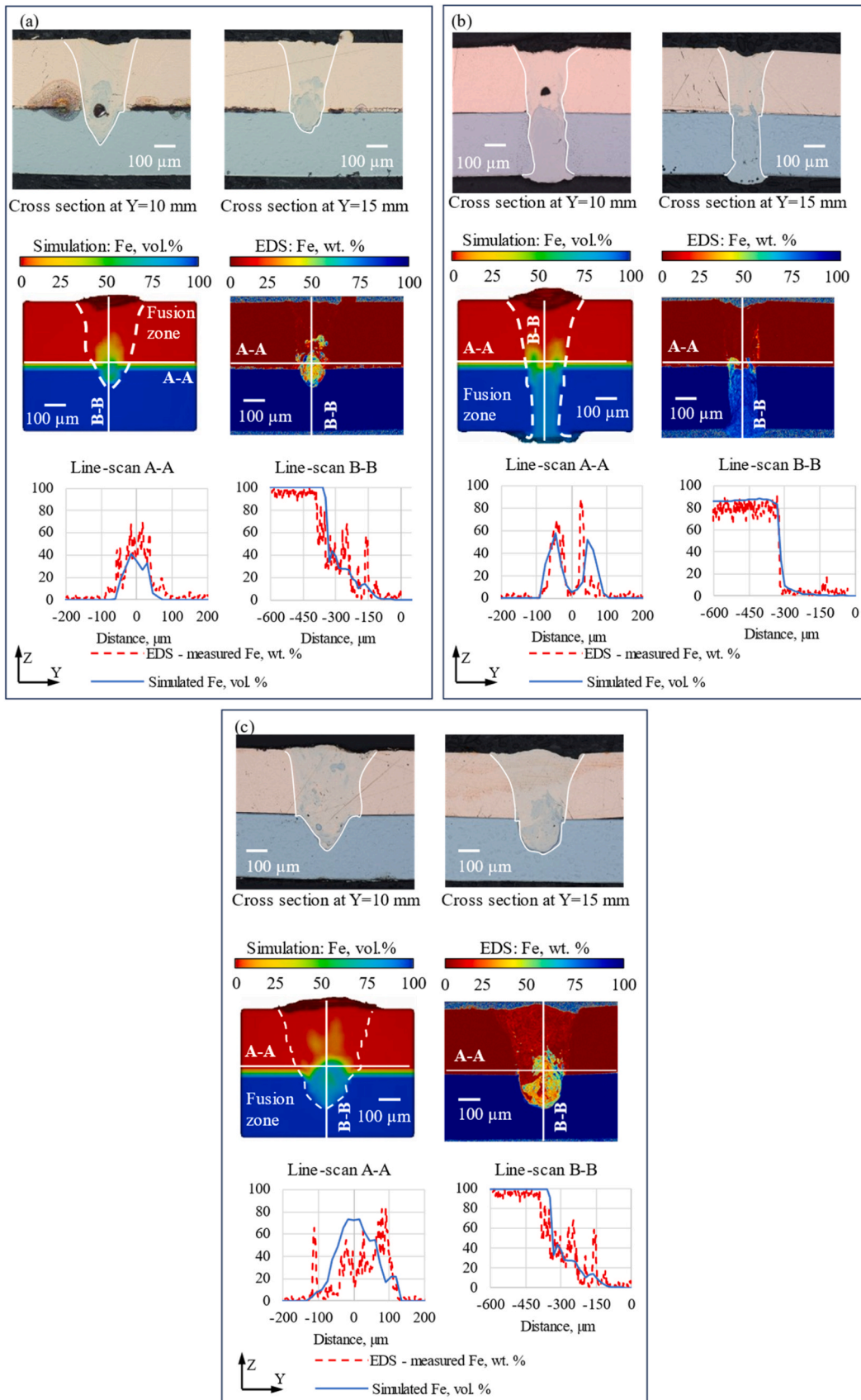**Fig. 5.** Temperature-dependent material properties defined in the model.

Fig. 6. Comparison of the experimental and modelling results of the molten pool geometry and elemental maps for weld configurations C1 (a), C2 (b) and C3 (c).

and validation process.

Fig. 6 shows cross sections and elemental maps for experiments C1, C2, and C3, and corresponding simulations. Two representative cross-sections from the same weld seam are shown in each sub-figure to demonstrate the capability of the model to reproduce the geometric shape and the mixing phaenomena at different longitudinal positions along the weld seam. The fusion zones are marked in each cross section and show good correlation with predictions from simulations, as the cases with partial penetration are successfully predicted in for C1 and C3, along with full penetration in C2.

Elemental maps that were measured with EDS, and species concentration that were predicted with simulations, are reported for comparison to show capability of the model to reproduce the mixing mechanism. For each case, plots of the concentration of Fe along with line-scans are reported to quantitatively demonstrate the capability of the model to simulated diffusion of the molten metal from the bottom sheet to the upper one. They show that diffusion of Fe in Cu is well predicted in C1 and C3, as well as presence of Fe-rich clusters in the Cu near the interface between parent materials is reproduced in C2.

Good correlation between measurements and predictions of the weld geometry and metal mixing demonstrates capability of the model to simulate welding scenarios with different laser beam shapes, and weld penetration depth spanning from partial penetration to full penetration. This allows to confidently deploy the simulation model in conjunction with experiments to study the impact of laser beam shaping on metal mixing and molten pool dynamics.

3.2. Keyhole dynamics and impact on metal mixing

As keyhole instabilities have a significant impact on weld quality (Lu et al., 2015), this section highlights the impact of the laser beam shapes on the keyhole dynamics, which ultimately contributes to metal mixing. The discussion is presented by linking the laser power profile to the velocity field within the molten pool and ultimately to the metal mixing between the parent metals and the occurrence of collapse events of the keyhole.

Fig. 7 shows consecutive time frames in each weld configuration and reflects keyhole dynamic mechanisms. The keyhole's shape and size vary, exhibiting irregularities, asymmetry and fluctuations. These shapes are directly correlated to the laser beam shape profile. The following observations are made:

- Collapse events terminate in formation of pores and metal mixing. This is visible in the experimental results presented in Fig. 6(a) and (b), where relatively large pores are observed in the experimental cross-section. With a narrow beam profile (weld configuration C1, C2, C3 and C5) and high energy density, once fusion of the Cu does happen, a surplus of energy flows through the keyhole, increasing the temperature at the keyhole bottom. This generates a recoil pressure that pushes the fluid upwards. At the top surface and rear
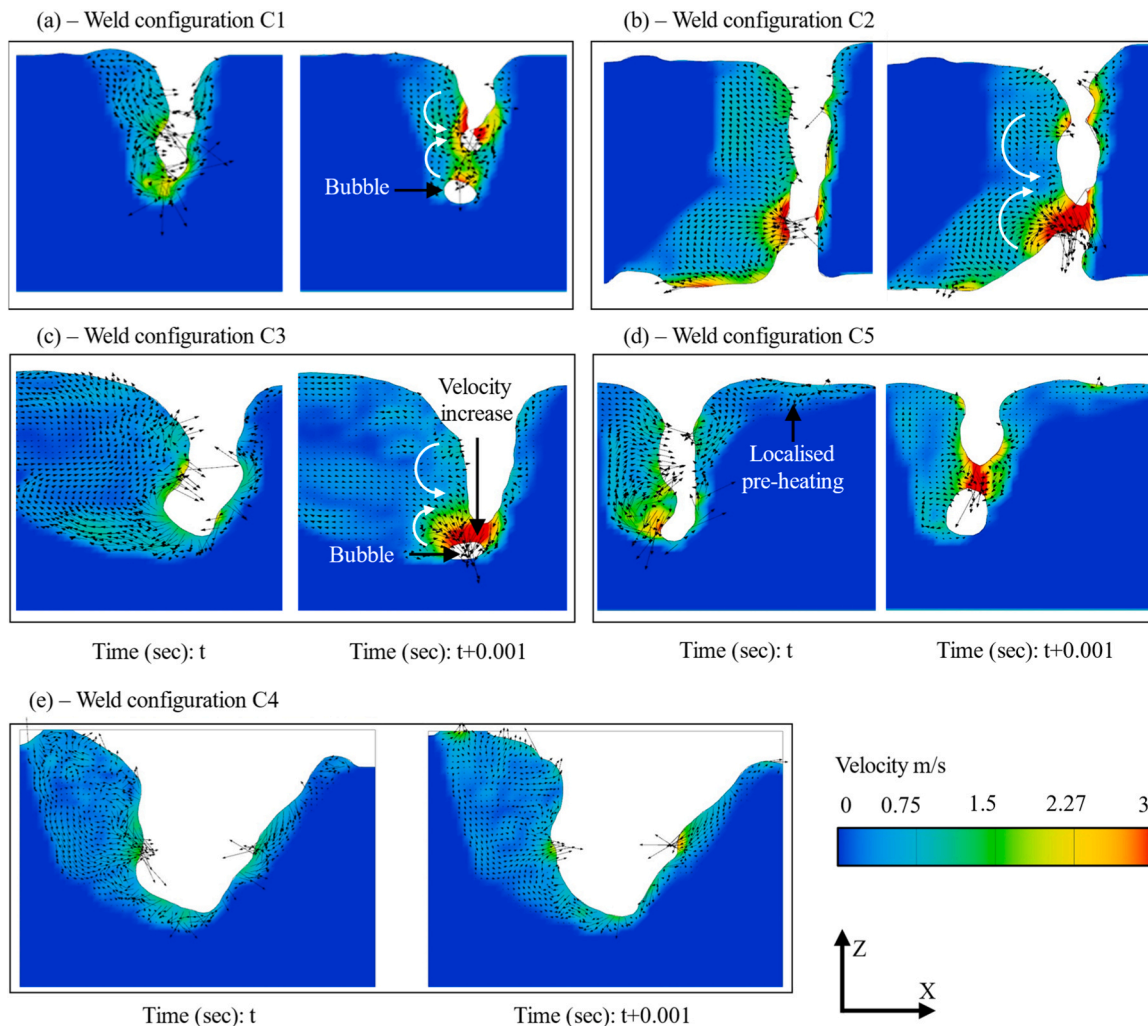

Fig. 7. Consecutive time steps of the molten pool dynamics for configuration C1 (a), C2 (b), C3 (c) C5 (d) and C4 (e). The plot shows the fluid velocity (both direction and magnitude) visualized by black arrows. Cross sections taken at Y= 0.

side of the keyhole, the opposing movements of the fluid, both clockwise and counter-clockwise, and driven by the Marangoni force, have an important consequence: they restrict the size of the molten pool. This restriction creates a high viscosity mushy layer that forms a barrier that limits the expansion of the molten pool. As result, closure or narrowing the top neck of the keyhole restricts the ejection of vapours out of keyhole which leads to increase in pressure within keyhole and creates a high-pressure lob. This ultimately results in pores formed to the toe of the keyhole as seen in Fig. 7(a) and (b). Although a collapse event is observed in C3 as shown Fig. 7(c), it does not necessarily create porosity in the solid front as sufficient room is available for gas vapours to escape from the bottom of the keyhole. The introduction of a pre-heat heating beam in weld configuration C5 does not produce any significant change to the keyhole dynamics as observed in Fig. 7(d). In partial penetration, narrow and deep keyhole is more unstable as slight fluctuations in fluid pressure, velocity and temperature on the rear wall of keyhole can create a collapse event. Additionally, the collapse of the keyhole in partial penetration creates a narrower fluid channel, resulting in localized increase of fluid velocity, which, in turn, affects metal mixing.

- Weld configuration C4 leads to wider opening of the keyhole with greater stability as shown in Fig. 7(e). With the super-imposition of the core beam with the wider ring-shaped beam, the core beam penetrates the steel sheet, while the larger ring keeps the keyhole open at the Cu surface. This weld configuration drastically reduces the collapse events and the development of bubbles. It can be observed that the lower depth-to-width aspect ratio of the melt pool correlates to fewer number of collapse events.

- Metal mixing is not only influenced by keyhole dynamics and collapse events, but there is an intricate interplay between keyhole geometry, fluid dynamics and buoyancy forces that are dependent upon density which varies with temperature in molten pool, and

from top to bottom due to differences in density between Cu and steel. To test the influence of buoyancy forces, a simulation test was performed where the density of Cu and steel were artificially set to be equal. Fig. 8 shows the simulation results and confirm that buoyancy forces have an impact on the metal mixing especially at the interface between the two metals and in the Cu side of the weld. For example, the line-scan B-B in Fig. 8 shows an increase on average of the Fe vol % in the Cu side by 10%, when comparing results with same densities.

The introduction of a ring beam (weld configuration C4 with LBS#3) in the laser welding process alters the shape of the keyhole compared to a single beam scenario (weld configuration C1 with LBS#1). In the single beam case, the keyhole walls develops predominantly in Z direction (schematically illustrated in Fig. 9(a)). The inclusion of a ring beam results in the critical change of the keyhole wall's curvature, with a pronounced arc-like shape at the rear (Fig. 9(b)). The change of keyhole wall's curvature plays a critical role and is explained by the complex equilibrium between the fluid pressure, the recoil pressure and the gravity load. A collapse event is associated with the non-equilibrium of the forces in the X direction. To explain this, it is first worth noting that with an idealised static molten pool (no fluid velocity) the fluid pressure would be higher at the bottom and would be governed by the hydrostatic law – with this, the pressure variation occurs linearly downwards and would be a function of the molten pool depth. Under this ideal condition, the keyhole would exhibit a stable equilibrium regime driven by the balanced effect of recoil pressure and fluid flow. With the actual molten pool, the equilibrium state is, however, perturbated by the non-linear variation of the fluid pressure due to the fast upwards motion generated by the recoil pressure itself. A near-equilibrium state is eventually achieved with the change of keyhole wall's curvature with the resultant of the forces acting predominantly in the Z direction. The shallow angle of the keyhole wall observed at LBS#3 ($\theta_3 < \theta_1$) effectively decomposes the combined forces exerted by the fluid towards the Z direction, hence moving to the near-equilibrium
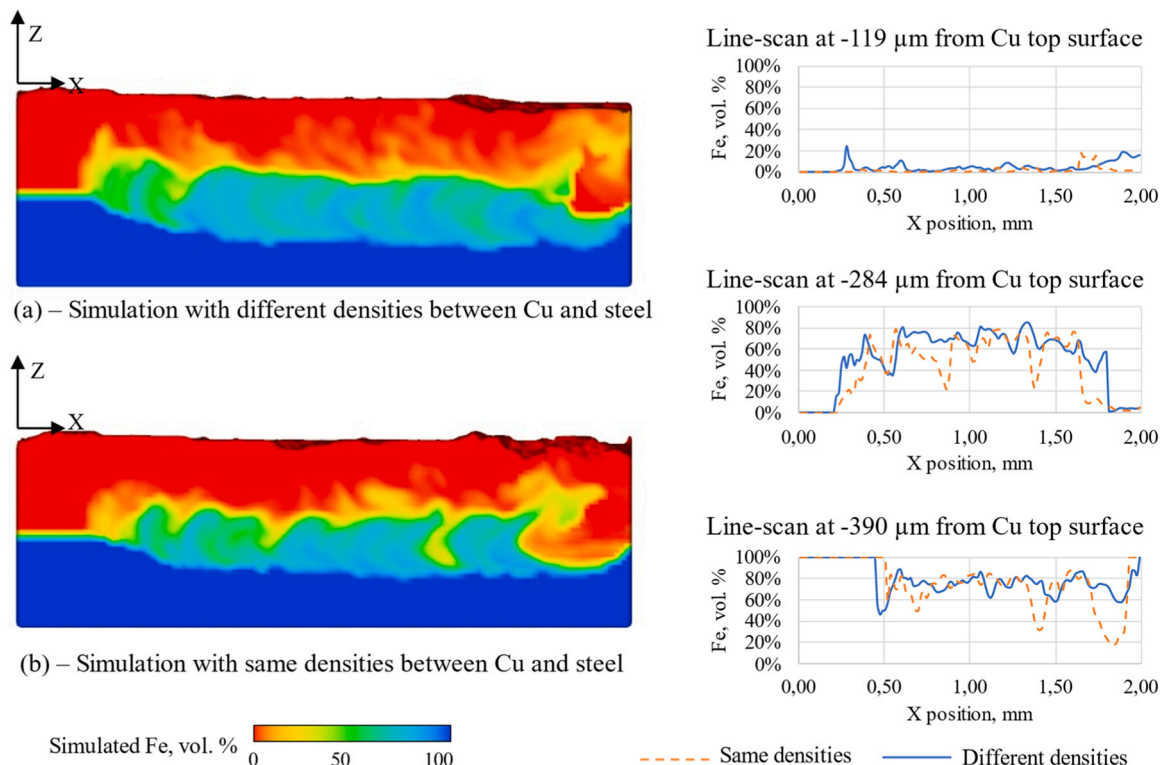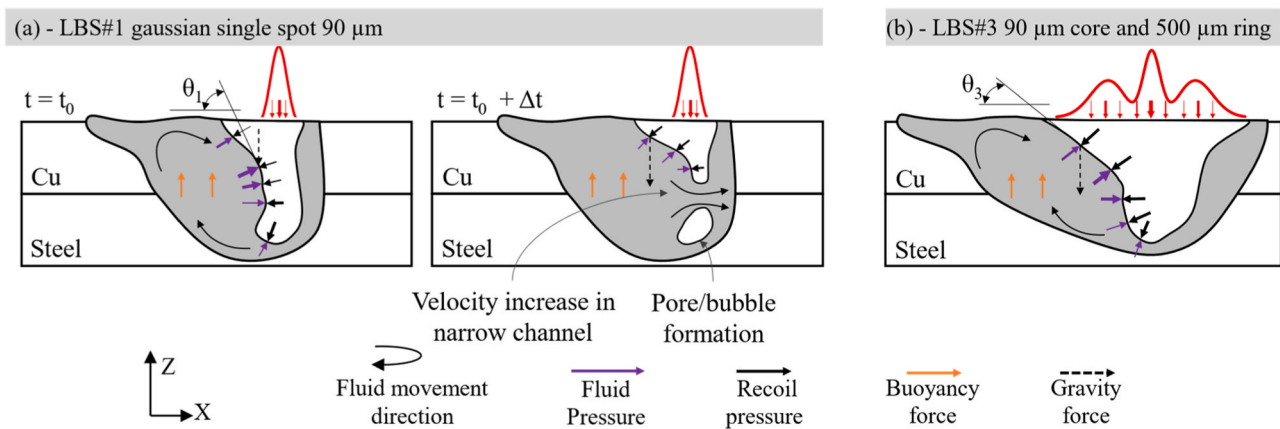

Fig. 8. Impact of buoyancy forces on the metal mixing for weld configuration C3. Sections taken at Y= 0.

Fig. 9. Schematic representation of forces and pressures acting on the melt pool in case of welding with single laser beam (LBS#1) and ring-core configuration (LBS#3). Arrows represent forces/pressures, and the thickness is proportional of the intensity of the forces/pressures. Arrows are only shown to the rear-side of the keyhole since the physics involved there are more relevant for the dynamics of the keyhole.

state, with the fluid pushed downwards in Z rather than sidewise in X. It can be observed that the ring-to-core diameter and the ring-to-core power are essential to control the keyhole wall's curvature and ultimately influence of the stability of the keyhole.

3.3. Impact of beam shaping on metal mixing

Cu and steel are generally immiscible as studied by other researchers, such as Shi et al. (2013). This separation means the material solidifies as two separate phases from the liquid state. At this immiscible region a Cu-rich (α phase) and iron-rich (β phase) form FCC and BCC crystal structures, respectively. For the compositional data shown in Fig. 6, the highest amount of mixing for each of the three examples is 60%, 80% and 50% of Fe in the weld pool. When studying the Cu-Fe binary phase diagram, as performed by Chen et al. (2007), these compositions fall within the miscibility gap range. For which no IMCs are expected to form, but instead separate (α and β) phases. However, it is still clear that the formation of these separate phases still creates a mismatch in mechanical properties of the welded joint, both at the interface and enriched regions, which can lead to crack initiation, as reported by Rinne et al. (2020). For this reason, analysing the metal-mixing in dissimilar metals is an important step toward understanding and prevention of cracking mechanisms that can affect the performance of the weld.

Influence of the beam shapes on the metal mixing, can be investigated by analysing velocity fields and fluid flow which are predicted with the validated model. Fig. 10(a) and (b) show that in the weld configuration C1 and C2 (corresponding to LBS#1 - single beam with circular spot and gaussian distribution) the increase in laser power leads to more steel mixing with Cu due to greater recoil pressure and to a larger melt pool with more liquid metal involved. When comparing the parameters in Fig. 11, the increased melting of the bottom steel sheet leads to a greater region of keyhole necking with collapse; this can be due to the increased laser absorption, for which steel has a greater absorptivity than the more reflective Cu (Rinne et al., 2020). The lower density of steel creates an upward buoyancy force which allows the migration of more steel into the Cu-rich region. Fig. 11(c) and (d) show weld configurations C3 and C4 respectively, with combined secondary ring-shaped and primary laser beam (LBS#2 and LBS#3, respectively). They can be compared based on similar levels of weld penetration but different width at the interface between parent metals and at the top of the weld seam. Spread of the laser power over a wider surface due to the use of a ring results in a wider weld pool compared to simulations C1 and C2, which is consistent with results found by Jabar et al. (2023). However, one difference between these two cases is that, due to different power density distributions, to achieve adequate weld penetration

depth, different laser power is provided leading to different thermal fields and time that the metal stays liquid. Line-scans of the temperature profiles in the melt pool can be observed in Fig. 12, with higher peak temperature in C4, compared to simulations C1 and C2, and C5; whereas a smaller secondary ring-shaped laser beam in simulation C3 results in intermediate behaviour.

The higher peak temperature in C4 eventually leads to a significant thermal gradient that promotes significant upward buoyancy forces and ultimately more migration of steel towards the Cu matrix. Similarity of simulation C5 with C1 can be explained considering that the secondary laser beam pre-heats the metal without widening the keyhole. Additionally, the higher peak temperature and larger size of the melt pool in C4 lead to longer time in which the steel stays in the liquid phase with more time available to migrate toward the Cu matrix due to recoil pressure and buoyancy forces and to diffuse. For these reasons, if use of larger spot helps with keyhole stabilisation, higher laser power required to establish sound connection enhances mixing between parent metal. Therefore, selection of custom ring-to-core diameter and ring-to-core power is a decision with a trade-off between the need of stabilising the keyhole dynamics and the need to reduce the mixing.

Velocity fields in Fig. 11 show also that the use of the ring-shaped secondary beam (C4), results in lower recoil pressure due to less localised laser power and vaporization. For this reason, the fluid flow and velocity of the liquid movements in considerably lower, as shown by contour plots, where regions of the molten pool in red are those in which the flow of the liquid metal is faster. The metal mixing in the molten pool of C3 weld is more homogeneous than in C1 and C2, due to the localised heat input of the ring laser beam. Rinne et al. (2020) found the addition of the ring laser produced a more homogeneous distribution of Cu and steel in the solidified structure. The lower density of the steel can also be used to explain the more even distribution of steel throughout the weld pool of C3. This is also confirmed by the EDS line-scans in Fig. 6(c) that show a significant drop of Fe into the Cu matrix compared to C1 (Fig. 6 (a)).

The result of metal mixing has a significant effect on the crack formation in the weld pool and heat-affected zone (HAZ). Two main types of cracking are often referred to as "hot cracking" (Rinne et al., 2020) or "liquation cracking" (Li et al., 2019). During any fusion welding process of Cu to steel the miscibility gap can be identified in the binary phase diagram of Cu-Fe (Chen et al., 2013). When both Cu and steel are melted, there is separation of the liquids during cooling, once the mixture enters the miscibility gap seen on the phase diagram the primary separation of the α and β phases occurs. The secondary separation occurs in the miscibility gap because of a lack of diffusion and a supersaturation of the α and/or β phases. The solidified weld microstructure is found
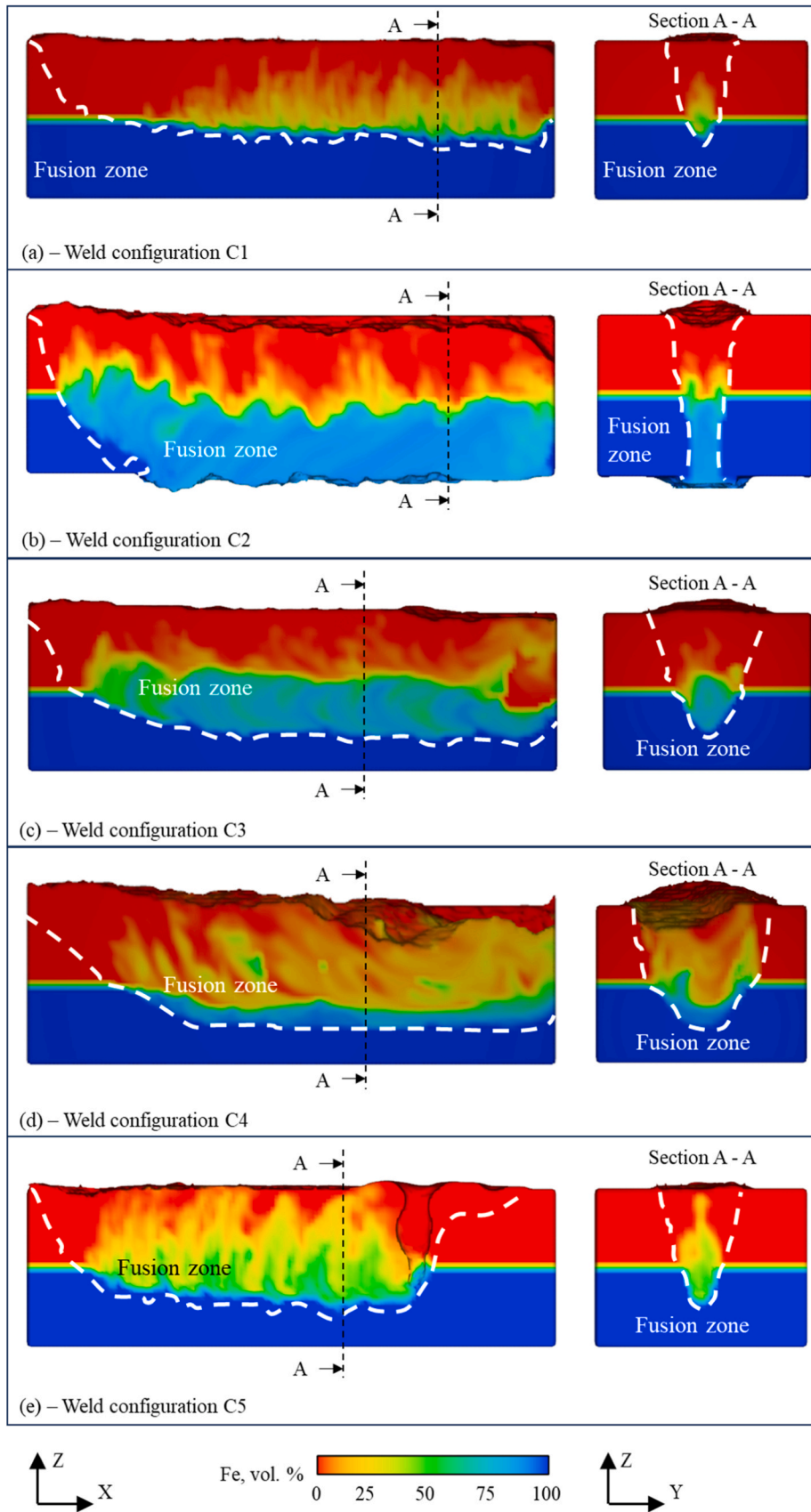
Fig. 10. Plots of metal mixing in the longitudinal and a cross sections predicted with simulations C1 (a), C2 (b), C3 (c), C4 (d) and C5 (e).
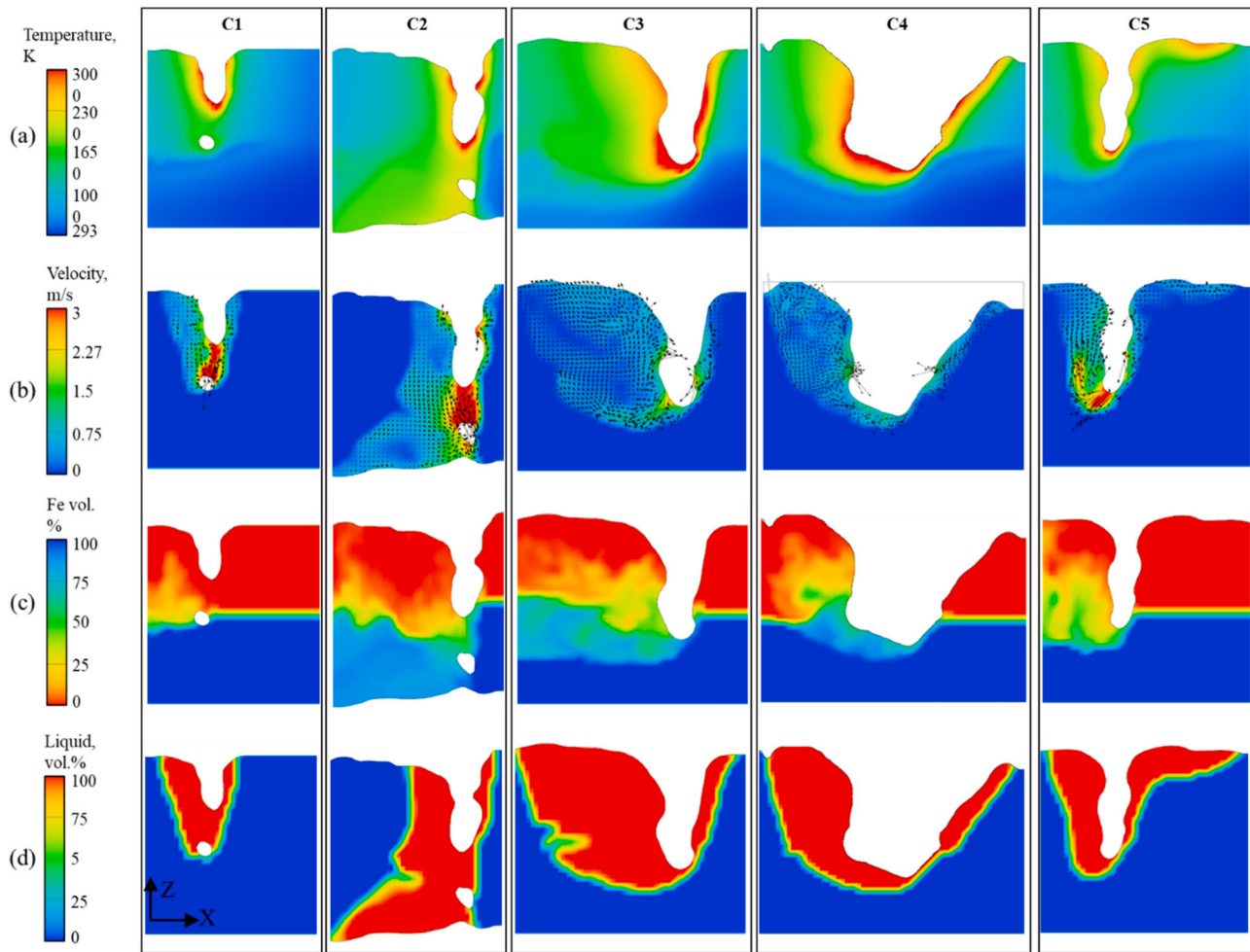
Fig. 11. (a) Temperature, (b) velocity, (c) Fe concentration and (d) actual melt pool for all the tested weld configurations C1 to C5. Cross sections taken at Y= 0.
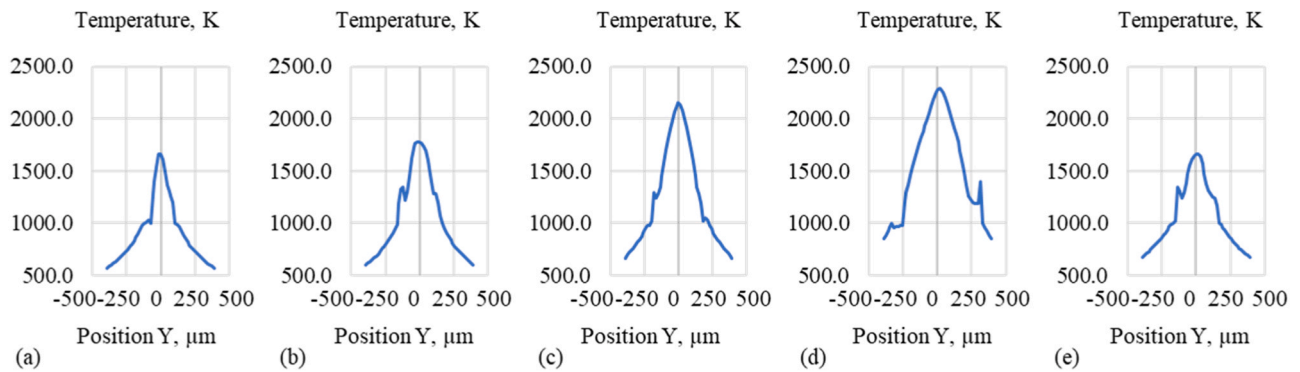

Fig. 12. Temperature profiles for weld configurations C1 (a), C2 (b), C3 (c), C4 (d) and C5 (e). Measurements were taken at X = 1.3 mm (just behind the keyhole wall) and Z = −300 μm (interface between Cu and steel).

inhomogeneous, consisting of the α and β phases. The difference in the thermal expansion properties of both Cu and steel can create locations of stress concentrations where cracks are often initiated, ad observed by Chen et al. (2013) and Sadeghian and Iqbal (2022). Li et al. (2019) proposed a three-stage mechanism for the formation of liquation cracks in Cu to steel laser welds. The first stage was the penetration of Cu liquid into the grain boundaries of the steel, secondly, the Cu liquid surrounds the Cu phase creating a "film" of liquid in the grain boundary. This drastically reduces the cohesive forces between the grain boundaries due to the presence of the α phase. Cracking can then be initiated in a

similar manner to that detailed earlier.

4. Conclusions

A combination of multi-physics CFD modelling results and experiments have been presented to study the impact of laser beam shaping on metal mixing and molten pool dynamics during LBW of Cu-to-steel for battery terminal-to-casing connections. The multi-physics model has been validated with *ex-situ* EDS element mapping and weld profile's features. The model has provided useful insights about temperature and

velocity fields, mixing mechanisms and dynamics of the keyhole, all of which are difficult to access via experiments due to technological difficulties. The major findings of the work are summarized below:

- Metal mixing is largely influenced by the fluid dynamics via the Marangoni, buoyancy forces and recoil pressure. With a greater laser power, recoil pressure is increased, and this leads to more weld penetration and melting of steel. Additionally, spread of the laser power results in higher width of the fusion zone. Subsequently, the buoyance forces due to the different densities of steel and Cu contribute to the upward flow of steel towards Cu, and hence impact meaningfully to the mixing. This can be clearly observed in weld configurations C1 and C2.
- Due to the collapse events of the keyhole wall, porosity formation was found in welds C1, C2 and C5. Furthermore, the collapse events create a narrow fluid channel, which results in localised surges in fluid velocity, therefore, promoting metal mixing. All in all, simulations revealed that increasing depth-to-width aspect ratio is correlated to higher frequency of collapse events in the keyhole. Therefore, stabilisation of the melt pool can be achieved with tailored laser beam shapes.
- The study has pointed-out that the use of larger ring beam (configuration C4) helps with keyhole stabilisation, but at the same time leads to more laser power and higher temperature that contribute to the enhancement of mixing between parent metals. This poses a trade-off in the definition of a tailored ring-to-core diameter and the ring-to-core power. Analysis of the results showed that ring-to-core diameter (350–90 μm) and 30% of ring power (weld configuration C3) resulted in more stable dynamics of the keyhole, with significant reduction of collapse events, and ultimately controlled migration of steel towards Cu. Furthermore, compared to C4 (2500 W total power), the lower thermal gradient in C3 (1530 W total power) eventually leads to a reduction in the upward buoyancy forces.
- The pre-heating approach with the tandem beam (C5) only led to local fusion of Cu and no significant improvement in keyhole stability was observed.

The combination of experiments and numerical modelling provides a powerful approach to understand complex fluid flow and metal mixing processes during laser keyhole welding. This helps to study mixing behaviour along with weld pool dynamics for selection of laser welding strategies with beam shaping in case of dissimilar material welding, especially in presence of miscibility gap at higher temperature as in case of Cu and steel.

CRediT authorship contribution statement

The authors confirm contribution to the paper as follows: **Giovanni Chianese**: Conceptualization, Methodology, Software, Validation, Formal analysis, Investigation, Data curation, Writing − original draft, Writing – review & editing, Visualization. **Qamar Hayat**: Conceptualization, Writing − original draft, Writing − review & editing, Visualization, Investigation, Writing − original draft preparation. **Sharhid Jabar**: Investigation, Writing − original draft, Writing − original draft preparation, Visualization, Writing − review & editing. **Pasquale Franciosa**: Conceptualization, Methodology, Validation, Formal analysis, Investigation, Resources, Writing – review & editing, Visualization, Supervision, Project administration, Funding acquisition. **Darek Ceglarek**: Resources, Writing – review & editing, Funding acquisition. **Stanislao Patalano:** Writing − review & editing, Funding acquisition, Supervision.

Declaration of Competing Interest

The authors declare that they have no known competing financial interests or personal relationships that could have appeared to influence the work reported in this paper.

Data availability

Data will be made available on request.

Acknowledgements

References

Brand, M.J., Schmidt, P.A., Zaeh, M.F., Jossen, A., 2015. Welding techniques for battery cells and resulting electrical contact resistances. J. Energy Storage 1, 7–14.

Buttazzoni, M., Zenz, C., Otto, A., Gómez Vázquez, R., Liedl, G., Arias, J.L., 2021. A numerical investigation of the laser beam welding of stainless steel sheets with a gap. Appl. Sci. 11, 2549.

Caprio, L., Previtali, B., Demir, A.G., 2023. Effect of in-source beam shaping and laser beam oscillation on the electromechanical properties of Ni-plated steel joints for e-vehicle battery manufacturing. J. Laser Appl. 35, 042030.

Chen, S., Huang, J., Xia, J., Zhang, H., Zhao, X., 2013. Microstructural characteristics of a stainless steel/copper dissimilar joint made by laser welding. Metall. Mater. Trans. A 44 (8), 3690–3696.

Chen, Y.Z., Liu, F., Yang, G.C., Xu, X.Q., Zhou, Y.H., 2007. Rapid solidification of bulk undercooled hypoperitectic Fe–Cu alloy. J. Alloy. Compd. 427 (1–2), L1–L5.

Chianese, G., Franciosa, P., Sun, T., Ceglarek, D., Patalano, S., 2022. Using photodiodes and supervised machine learning for automatic classification of weld defects in laser welding of thin foils copper-to-steel battery tabs. J. Laser Appl. 34, 042007.

Chianese, G., Jabar, S., Franciosa, P., Ceglarek, D., Patalano, S., 2022. A multi-physics CFD study on the part-to-part gap during remote laser welding of copper-to-steel battery tab connectors with beam wobbling. Procedia CIRP 111, 484–489.

Daligault, J., Dal, M., Gorny, C., Coste, F., Fabbro, R., 2022. Combination of Eulerian and ray-tracing approaches for copper laser welding simulation. J. Laser Appl. 34, 042042.

Das, A., Li, D., Williams, D., Greenwood, D., 2018. Joining Technologies for Automotive Battery Systems Manufacturing. World Electr. Veh. J. 9 (2), 22.

Drobniak, P., Otto, A., Vázquez, R.G., Arias, R.M., Arias, J.L., 2020. Simulation of keyhole laser welding of stainless steel plates with a gap. Procedia CIRP 94, 731–736.

Hao, Y., Chen, N., Wang, H., Carlson, B.E., Lu, F., 2021. Effect of zinc vapor forces on spattering in partial penetration laser welding of zinc-coated steels. J. Mater. Process. Technol. 298, 117282.

Huang, W., Wang, H., Rinker, T., Tan, W., 2020. Investigation of metal mixing in laser keyhole welding of dissimilar metals. Mater. Des. 195, 109056.

Huang, W., Cai, W., Rinker, T.J., Bracey, J., Tan, W., 2023. Effects of laser oscillation on metal mixing, microstructure, and mechanical property of Aluminum–Copper welds. Int. J. Mach. Tools Manuf. 188, 104020.

Hummel, M., Schöler, C., Häusler, A., Gillner, A., Poprawe, R., 2020. New approaches on laser micro welding of copper by using a laser beam source with a wavelength of 450 nm. J. Adv. Join. Process. 1, 100012.

IEA , 2022: Global EV Outlook 2022 - Securing supplies for an electric future, 2022.

Jabar, S., Barenji, A.B., Franciosa, P., Kotadia, H.R., Ceglarek, D., 2023. Effects of the adjustable ring-mode laser on intermetallic formation and mechanical properties of steel to aluminium laser welded lap joints. Mater. Des. 227, 111774.

Jeong, Y.B., Jo, H.R., Park, H.J., Kato, H., Kim, K.B., 2020. Mechanical properties and microstructural change in (Cu–Fe) immiscible metal matrix composite: Effect of Mg on secondary phase separation. J. Mater. Res. Technol. 9 (6), 15989–15995.

Kogel-Hollacher, M., 2020. The full potential of Photonics in e-mobility: an overwiev. Laser Use 97, 22–23.

Kogel-Hollacher, M., Nicolay, T., Reiser, J., 2022, Going Green - Laser Welding and Advanced Sensor Technology for Electric Vehicles.

Kumar, N., Masters, I., Das, A., 2021. In-depth evaluation of laser-welded similar and dissimilar material tab-to-busbar electrical interconnects for electric vehicle battery pack. J. Manuf. Process. 70, 78–96.

Li, J., Cai, Y., Yan, F., Wang, C., Zhu, Z., Hu, C., 2019. Porosity and liquation cracking of dissimilar Nd:YAG laser welding of SUS304 stainless steel to T2 copper. Opt. Laser Technol. 122, 105881.

Lin, R., Wang, H., Lu, F., Solomon, J., Carlson, B.E., 2017. Numerical study of keyhole dynamics and keyhole-induced porosity formation in remote laser welding of Al alloys. Int. J. Heat. Mass Transf. 108 (A), 244–256.

Liu, Z., Wang, X., Hang, K., 2019. Enhancement of trapping efficiency by utilizing a hollow sinh-Gaussian beam. Sci. Rep. 9, 10187.

Lu, F., Li, X., Li, Z., Tang, X., Cui, H., 2015. Formation and influence mechanism of keyhole-induced porosity in deep-penetration laser welding based on 3D transient modeling. Int. J. Heat. Mass Transf. 90, 1143–1152.

Perez Zapico, E., Ascari, A., Dimatteo, V., Fortunato, A., 2021. Laser dissimilar welding of copper and steel thin sheets for battery production. J. Laser Appl. 33 (1), 012016.

Prieto, C., Vaamonde, E., Diego-Vallejo, D., Jimenez, J., Urbach, B., Vidne, Y., Shekel, E., 2020. Dynamic laser beam shaping for laser aluminium welding in e-mobility applications. Procedia CIRP 94, 596–600.

Rinne, J., Nothdurft, S., Hermsdorf, J., Kaierle, S., Overmeyer, L., 2020. Advantages of adjustable intensity profiles for laser beam welding of steel copper dissimilar joints. Procedia CIRP 94, 661–665.

Rinne, J., Nothdurft, S., Hermsdorf, J., Kaierle, S., Overmeyer, L., 2022. Multivariate parametric study on laser beam welding of copper lap joints using adjustable intensity profiles. Procedia CIRP 111, 415–419.

Sadeghian, A., Iqbal, N., 2022. A review on dissimilar laser welding of steel-copper, steel-aluminum, aluminum-copper, and steel-nickel for electric vehicle battery manufacturing. Opt. Laser Technol. 146, 107595.

Shi, R.P., Wang, C.P., Wheeler, D., Liu, X.J., Wang, Y., 2013. Formation mechanisms of self-organized core/shell and core/shell/corona microstructures in liquid droplets of immiscible alloys. Acta Mater. 61 (4), 1229–1243.

Sokolov, M., Franciosa, P., Sun, T., Ceglarek, D., Dimatteo, V., 2021. Applying optical coherence tomography for weld depth monitoring in remote laser welding of automotive battery tab connectors. J. Laser Appl. 33 (1), 012028.

Wagner, J., Heider, A., Ramsayer, R., Weber, R., Faure, F., Leis, A., Armon, N., Susid, R., Tsiony, O., Shekel, E., Graf, T., 2022. Influence of dynamic beam shaping on the geometry of the keyhole during laser beam welding. Procedia CIRP 111, 448–452.

Zwicker, M.F.R., Moghadam, M., Zhang, W., Nielsen, C.V., 2020. Journal of Advanced Joining Processes Automotive battery pack manufacturing – a review of battery to tab. J. Adv. Join. Process. 1, 100017.